TECHNICAL ADVANCE

Natural products in *Glycyrrhiza glabra* (licorice) rhizome imaged at the cellular level by atmospheric pressure matrix-assisted laser desorption/ionization tandem mass spectrometry imaging

Bin Li[1,2,†], Dhaka Ram Bhandari[1,†], Christian Janfelt[2], Andreas Römpp[1] and Bernhard Spengler[1,*]

[1]*Institute of Inorganic and Analytical Chemistry, Justus Liebig University Giessen, Schubertstrasse 60, building 16, 35392 Giessen, Germany, and*
[2]*Department of Pharmacy, University of Copenhagen, Universitetsparken 2, 2100 Copenhagen, Denmark*

SUMMARY

The rhizome of *Glycyrrhiza glabra* (licorice) was analyzed by high-resolution mass spectrometry imaging and tandem mass spectrometry imaging. An atmospheric pressure matrix-assisted laser desorption/ionization imaging ion source was combined with an orbital trapping mass spectrometer in order to obtain high-resolution imaging in mass and space. Sections of the rhizome were imaged with a spatial resolution of 10 μm in the positive ion mode, and a large number of secondary metabolites were localized and identified based on their accurate mass and MS/MS fragmentation patterns. Major tissue-specific metabolites, including free flavonoids, flavonoid glycosides and saponins, were successfully detected and visualized in images, showing their distributions at the cellular level. The analytical power of the technique was tested in the imaging of two isobaric licorice saponins with a mass difference of only 0.02 Da. With a mass resolving power of 140 000 and a bin width of 5 ppm in the image processing, the two compounds were well resolved in full-scan mode, and appeared with different distributions in the tissue sections. The identities of the compounds and their distributions were validated in a subsequent MS/MS imaging experiment, thereby confirming their identities and excluding possible analyte interference. The use of high spatial resolution, high mass resolution and tandem mass spectrometry in imaging experiments provides significant information about the biosynthetic pathway of flavonoids and saponins in legume species, combing the spatially resolved chemical information with morphological details at the microscopic level. Furthermore, the technique offers a scheme capable of high-throughput profiling of metabolites in plant tissues.

Keywords: AP-MALDI imaging, flavonoids, saponins, *Glycyrrhiza glabra*, high spatial resolution, technical advance.

INTRODUCTION

The localization of metabolites in plants is important, both in order to understand the functioning of the plant at the fundamental level and in the possible exploitation of natural products, e.g. in pharmaceutical or food products. Traditionally, such information has been obtained by the staining of tissue sections with various dyes in solution followed by visual inspection, typically with a microscope. These dyes react more or less specifically with cellular components, generating an optical contrast as an indication that certain compounds are present. For example, zinc chloride iodide is used for the staining of cellulose, Prussian blue is used for iron and tetrazolium is used for dehydrogenases, thus revealing the distribution of such compounds relative to the morphological structures of the tissue (Rogers, 1953). The histochemical methods are extensively applied in the localization of proteins in plant

tissues, as they are quick, cheap and informative (Jensen, 1962). Although histochemistry provides significant details about the organization of tissues, the approach is non-specific to metabolites and involves a risk of modified sample morphology and chemistry. The histochemistry of small molecules is even more problematic, as they are often relocated as a result of diffusion in water or solubility in organic solvents. Immunohistology, based on the binding of antibodies to antigens, offers more sensitive and specific spatial information than that obtained by the traditional morphological observations, but the complexity of the tool requiring highly specific antibodies for each target compound makes it a low-throughput and very costly approach, with regards to the number of compounds being imaged (Walker *et al.*, 2001). Additionally, interference of background staining and antigen–antibody cross-reactions can seriously affect the interpretation of the immunologic reaction (Ramos-Vara, 2005). Laser capture microdissection (LCM) combined with LC–MS (Abbott *et al.*, 2010; Yi *et al.*, 2012; Liang *et al.*, 2013) is an alternative way to profile secondary metabolites in specific cell types. LCM uses a highly focused infrared laser beam for the very accurate dissection of tissue, but the process is tedious and time-consuming, and does not offer a holistic view of the distribution of metabolites. Magnetic resonance imaging (MRI) has been used as a non-destructive technique to localize components in living plant tissues, but an accurate chemical specificity is still lacking (Borisjuk *et al.*, 2012).

Mass spectrometry-based imaging (MSI) techniques have been proven as powerful tools for exploring the spatial distribution of molecules in various materials (Schwamborn and Caprioli, 2010; Kaspar *et al.*, 2011). MSI is a family of label-free analytical techniques to create ion images of components corresponding to the distribution of molecular species in tissues. In MSI techniques, analytes are ionized from the sample surface, and mass spectra are recorded from a large set of spots throughout the surface. Thereby, the MSI techniques benefit from the chemical specificity of mass spectrometry and allow us to generate molecular images of hundreds of analytes in one experiment; with such a vast quantity of information available one can address the issues in complex biosystems from many different perspectives. The most common ionization techniques in MSI are matrix-assisted laser desorption/ionization (MALDI), desorption electrospray ionization (DESI) and secondary ion mass spectrometry (SIMS). The advent of these ionization techniques allows us to analyze both small molecules and macromolecules in complex solid biological materials.

The quality of *m/z* images depends upon several critical parameters, such as the spatial resolution, the mass spectral data as well as the sample preparation method. A long-standing technical challenge in MSI is the improvement of the spatial resolution down to cellular or even subcellular level. In DESI imaging, which indeed has some advantages with regards to the ease of sample preparation, the spatial resolution is restricted to approximately 100–200 μm because of the difficulty in focusing the ionizing spray spot, although a spatial resolution of 35 μm was recently obtained by careful optimization of several experimental parameters (Campbell *et al.*, 2012). MALDI imaging is by far the most commonly used MSI technique, introduced in the mid 1990s (Spengler *et al.*, 1994), and is now available on a number of commercial instruments. The spatial resolution that can be obtained with MALDI imaging is higher than that obtained with DESI, as MALDI imaging is typically performed with a spatial resolution of 50–100 μm, and under optimized conditions can get down to 3–5 μm, but the application of the matrix is a critical and complicated step that needs to be considered in the MALDI imaging. SIMS is known to provide a spatial resolution down to 50 nm, thus enabling imaging at the subcellular level (Guerquin-Kern *et al.*, 2005). The so-called useful lateral resolution of SIMS, which is defined by the limit of detection, however, is typically in the range of 1 μm for biomolecules from biological tissue. This resolution is superior to all other MS imaging techniques, but the price for it is strong fragmentation, which prevents the imaging and identification of most complex molecules, such as metabolites. Furthermore, besides the spatial resolution, the quality of the recorded mass spectra is important for imaging analysis, in terms of mass accuracy, spectral resolution and reliability. Low mass resolution results in the overlapping of neighboring mass peaks and loss of selectivity. Several experiments of MS imaging of metabolites were performed on low-resolution mass spectrometers, such as ion traps, resulting in the ambiguous identification of metabolites when no standard is available (Li *et al.*, 2011, 2013). Although the spectral resolution is important for the selectivity of the imaging analysis, the mass accuracy is important in the identification of the imaged analytes, as the accurate mass can be used to obtain the elementary formula of the analyte. The time-of-flight (TOF) analyzer can provide reasonable resolving power of up to 40 000 in reflection mode, and mass accuracy can be better than 5 ppm (Lee *et al.*, 2012). Imperfect sample flatness of biological samples and surface charging effects can deteriorate mass accuracy and specificity in TOF-MS. Although the mass resolution is not as high as in other high-resolution instruments, TOF-MS has an advantage in its high scan speed. It should be noted here that the tandem MS experiments cannot be performed with a single TOF mass analyzer, but only with the application of a TOF-TOF or Q–TOF set-up. Fourier transform ion cyclotron resonance (FT-ICR) and orbital trapping mass spectrometers have become popular choices for MSI experiments because of their ultra-high mass resolving power of more than 100 000 and their mass accuracies of better than 1 ppm, although at the

expense of longer scan times, compared with TOF instruments.

We have recently developed an atmospheric-pressure MALDI (AP-MALDI) ion source (Koestler *et al.*, 2008), which has been coupled to an orbital trapping mass spectrometer in order to obtain MALDI imaging with high spatial resolution, high mass spectral resolution and high mass accuracy for the metabolite profiling of biological samples (Römpp *et al.*, 2010). The significant instrumental improvements enable a spatial resolution down to the cellular level (Bouschen *et al.*, 2010; Schober *et al.*, 2012). The application of the Q–Exactive Orbitrap mass spectrometer allows for reliable metabolite profiling with high mass accuracy, in parallel with MS/MS imaging experiments at a scan speed of 1.3 s pixel^{-1} that also enables the imaging of relatively large areas. Phospholipids, peptides and drug compounds have been imaged in a number of tissue samples at a spatial resolution of 3–10 μm (Römpp and Spengler, 2013). In other experiments with the same experimental set–up, metabolites and lipids were imaged from individual cells (Schober *et al.*, 2012).

Most MS imaging studies so far have focused on its application for the imaging of mammalian tissues; however, recent studies have also proven the potential of the techniques in the localization of metabolites in plants, thereby taking plant science beyond classical botanic histochemistry (Burrell *et al.*, 2007; Robinson *et al.*, 2007; Ye *et al.*, 2013). Until now, most MALDI imaging experiments on plant tissue have been performed with a spatial resolution of 50–200 μm (Lee *et al.*, 2012; Svatoš and Mock, 2013; Bjarnholt *et al.*, 2014), and only a few examples of MALDI imaging of plant material with a resolution of 12 μm have been presented (Jun *et al.*, 2010). Therefore, in this study we implement mass spectrometry imaging with high resolution in mass and space for investigating the distributions of major natural products from *Glycyrrhiza glabra* (licorice), a well-known traditional herbal medicine. Licorice has been used in herbal remedies since prehistoric times. Experimental studies of this plant have revealed various pharmacological activities, such as anti-inflammatory, antimicrobial, antiviral, antiprotozoal, antioxidative, hepatoprotective and antitumor activities. A number of reviews (Fenwick *et al.*, 1990; Asl and Hosseinzadeh, 2008) have been published that elucidate the benefits of licorice as a medicinal plant. Additionally, it is used as a flavoring agent in the confectionery industry, and as a vital ingredient in cough mixtures and throat lozenges. Licorice is generally cultivated for its rhizomes (underground stems), which contain large quantities of glycyrrhizin, a sweet-tasting compound 50 times sweeter than sugar. The major active components in licorice include flavonoids (e.g. liquiritin apioside, isoviolanthin), chalcones (e.g. isoliquiritin), isoflavans (e.g. glabridin) and triterpene saponins (e.g. glycyrrhizic acid, licorice saponin G2/J2/B2) (Farag *et al.*, 2012).

These compounds are produced in relatively high concentrations and have biological activity not only as medicine but also as plant defense chemicals. Although a number of bioactive secondary metabolites have been isolated and identified from licorice, the location of licorice saponins (LSs) and flavonoids are poorly reported (Hayashi *et al.*, 1988, 1996; Shan *et al.*, 2001).
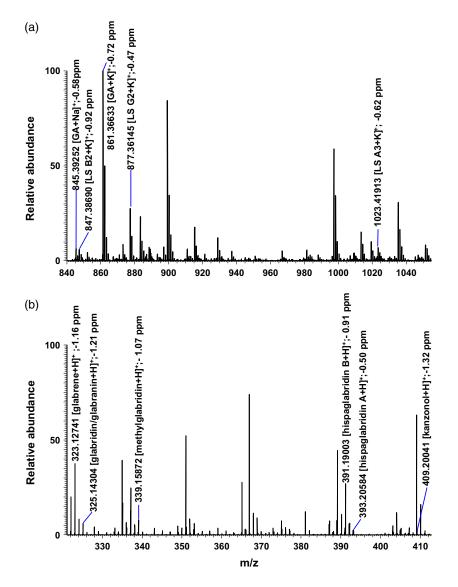
In this work, a number of metabolites were localized by AP–MALDI MS–based imaging. The results are in accordance with a few earlier histochemical studies (Hayashi *et al.*, 1988, 1996; Shan *et al.*, 2001), but more detailed information is added by the use of high-resolution MS imaging. The distribution maps of several natural products presented here, especially for the class of licorice flavonoids, provide significant hints that can be correlated with the histological and metabolic features of licorice, because the specialized physiologies of anatomically distinct components contribute to their specific biofunctions. Moreover, the *m/z* images of metabolites in licorice offer information of importance in studies of metabolite transport between spatially discrete compartments, as well as about biosynthesis and accumulation in different compartments and tissues.

RESULTS

AP–MALDI imaging of major metabolites in rhizome sections of licorice

Figure 1 shows representative mass spectra obtained from the licorice rhizome. Licorice saponins were mainly detected as sodium- and potassium-adduct ions (Figure 1a), around *m/z* 800–1050, and the flavonoids were readily detected as protonated ions in positive-ion mode in the low mass region (Figure 1b). The identities of the compounds were verified by accurate mass and/or tandem MS measurements, depending on the signal intensity; at very low ion abundances, the accurate mass was always available, whereas the ion abundance was eventually too low for an MS/MS spectrum to be recorded.

Figure 2 shows ion images of various metabolites in the rhizome section. A number of flavonoids were detected, in particular at the cork layer of the rhizome (Figure 2b), including glabrene (*m/z* 323.12779, $[C_{20}H_{18}O_4+H]^+$), licoagroaurone (*m/z* 339.12270, $[C_{20}H_{18}O_5+H]^+$), methylglabridin/licochalcone A/licochalcone C (*m/z* 339.15909, $[C_{21}H_{22}O_4+H]^+$), hispaglabridin B (*m/z* 391.19039, $[C_{25}H_{26}O_4+H]^+$), hispaglabridin A/glabrol (*m/z* 393.20604, $[C_{25}H_{28}O_4+H]^+$), 3–hydroxyglabrol (*m/z* 409.20095, $[C_{25}H_{28}O_5+H]^+$), kanzonol Y (*m/z* 411.21660, $[C_{25}H_{30}O_5+H]^+$) and licoagrodin (*m/z* 729.30581, $[C_{45}H_{44}O_9+H]^+$). Flavonoid glycosides such as liquiritin/neoliquiritin/isoliquiritin/neoisoliquiritin (*m/z* 457.08954, $[C_{21}H_{22}O_9+K]^+$), liquiritin apioside/isoliquiritin apioside/licuroside (*m/z* 589.13180, $[C_{26}H_{30}O_{13}+K]^+$), schaftoside/isoschaftoside (*m/z* 603.11106, $[C_{26}H_{28}O_{14}+K]^+$) and isoviolanthin (*m/z* 617.12672, $[C_{27}H_{30}O_{14}+K]^+$) were detected with high

(a)

100

Relative abundance

845.39252 [GA+Na]+;-0.58ppm

847.38690 [LS B2+K]+;-0.92 ppm

861.36633 [GA+K]+;-0.72 ppm

877.36145 [LS G2+K]+;-0.47 ppm

1023.41913 [LS A3+K]+; -0.62 ppm

50

0

840 860 880 900 920 940 960 980 1000 1020 1040

(b)

100

Relative abundance

323.12741 [glabrene+H]+ ;-1.16 ppm

325.14304 [glabridin/glabranin+H]+;-1.21 ppm

339.15872 [methylglabridin+H]+; 1.07 ppm

391.19003 [hispaglabridin B+H]+;- 0.91 ppm

393.20584 [hispaglabridin A+H]+;-0.50 ppm

409.20041 [kanzonol+H]+;-1.32 ppm

50

0

330 340 350 360 370 380 390 400 410

m/z

Figure 1. (a) Single-pixel mass spectrum of saponins from the inner part of the *Glycyrrhiza glabra* (licorice) rhizome.
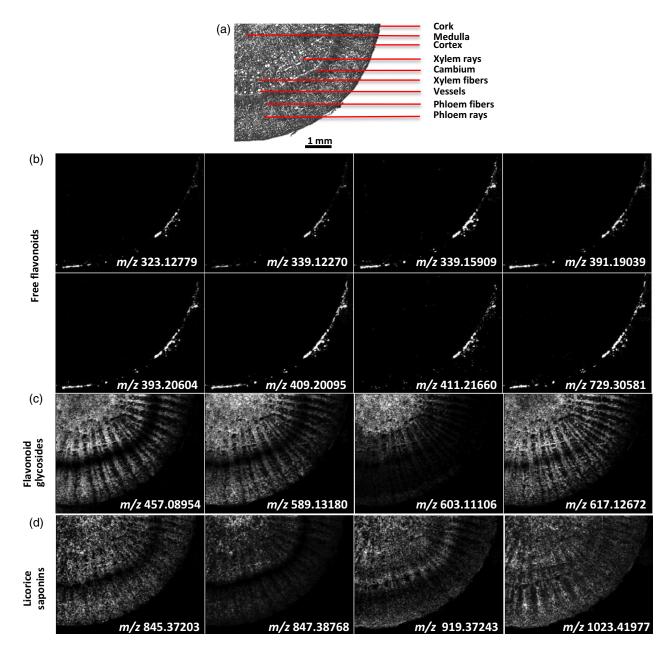(b) free flavonoids from the outside layer of the rhizome. The pixel size was 30 μm.

abundances in the internal parts, such as medulla, xylem and phloem rays, next to the cork layer of the rhizome (Figure 2c). The distribution of flavonoids in the licorice rhizome provides significant hints for understanding the defense functions of aglycones and related glycosides. In previous reports, similar distribution patterns of flavonoids had been observed in the root tissues of other herbal plants, such as *Scutellaria baicalensis* (Tani *et al.*, 1985), *Pueraria* (Tani *et al.*, 1986) and *Sophora flavescens* (Yamamoto *et al.*, 1992). The roles of flavonoids have been extensively explored, and they appear to constitute a class of vital defense metabolites in legume species (Graham *et al.*, 1990; Stafford, 1997). With the use of high spatial resolution MS-based imaging techniques, more precise spatial localizations of individual metabolites are gained compared with the histochemical methods. These MS images will contribute to the understanding of the ecophysiological role of flavonoids in leguminous tissues, such as defense against other organisms and symbiotic relationships with nitrogen-fixing bacteria.

Additionally, the four selected ions of saponins LS C2 (*m/z* 845.37203, $[C_{42}H_{62}O_{15}+K]^+$), LS B2 (*m/z* 847.38768 $[C_{42}H_{64}O_{15}+K]^+$), 22–acetoxyglycyrrhizin (*m/z* 919.37243, $[C_{44}H_{64}O_{18}+K]^+$) and LS A3 (*m/z* 1023.41977, $[C_{48}H_{72}O_{21}+K]^+$) found in the rhizome section showed similar distribution patterns. The LSs selected tended to accumulate more in the cork layer, cortex, phloem and xylem parts, as well as in the central pith, whereas they were absent in the cambium (Table 1).

The results obtained are consistent with previous studies indicating that saponins and flavonoids are not uniformly distributed in the rhizomes (Hayashi *et al.*, 1988, 1996), although details of this distribution were not well known. In order to obtain cellularly resolved localization of metabolites in the rhizome, additional MALDI imaging experiments were performed at a higher spatial resolution of 10 μm in an experiment with a run time of approximately 15 h. Figure 3 shows the resulting high-resolution MALDI images of three significant and representative compounds,

Figure 2. MALDI images of the *Glycyrrhiza glabra* (licorice) rhizome, recorded with a pixel size of 30 μm and 255 × 205 pixels in the image. The mass accuracy was better than 2 ppm (RMS), and a bin width of $m/z = \pm5$ ppm was used.
(a) Optical image of the rhizome.
(b) Free flavonoids.
(c) Flavonoid glycosides.
(d) Licorice saponins. Each individual image represents the protonated compounds or the sodium or potassium adducts of the compounds included in Table 1.
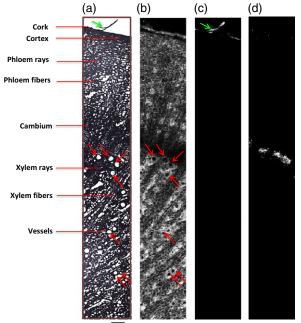
glycyrrhizic acid (GA) (m/z 861.36695, $[C_{42}H_{62}O_{16}+K]^+$), glabridin (m/z 325.14344, $[C_{20}H_{20}O_4+H]^+$) and PC(34:1) (m/z 798.54096, $[C_{42}H_{82}NO_8P+K]^+$). As seen in Figure 3(b), GA is mainly located in the cork layer, cortex, phloem and xylem parts, but is almost absent in the cambium layer. A relatively high content of GA was observed in phloem and xylem fibers compared with their neighboring cells. These distribution patterns are in accordance with previous reports that GA was mainly localized in the woody parts of thickened roots (Hayashi *et al.*, 1988; Shan *et al.*, 2001; Hayashi, 2009). In addition, glabridin, a prenylated isoflavonoid, is found exclusively in the cork layer of *G. glabra* (Figure 3c), with the same distribution pattern as for the other free flavonoids presented in Figure 2(b). The tiny part of the cracked cork layer (marked with a green arrow in Figure 3a and c) is clearly resolved at this high spatial

Table 1 Selected metabolites assigned in *Glycyrrhiza glabra* rhizome tissues by AP–MALDI MS imaging at a pixel size of 30 µm

Compounds	Aglycone class	Molecular formula	Theoretical monoisotopic mass (u)	Measured [M + H]+ (u) [theoretical monoisotopic mass (u), MS (ppm)]	Measured [M + Na]+ (u) [theoretical monoisotopic mass (u), RMS (ppm)]	Measured [M + K]+ (u) [theoretical monoisotopic mass (u), RMS (ppm)]
Glabrene	Isoflavene	$C_{20}H_{18}O_4$	322.12051	323.12758 (323.12779, 0.76)	345.10957 (345.10973, 1.36)	361.08346 (361.08367, 1.11)
Licoagroaurone	Aurone	$C_{20}H_{18}O_5$	338.11543	339.12255 (339.12270, 1.20)	361.10449 (361.10465, 1.38)	377.07839 (377.07858, 1.75)
Methylglabridin	Isoflavan	$C_{21}H_{22}O_4$	338.15181	339.15892 (339.15909, 0.76)	361.14051 (361.14103, 2.97[a])	377.11495 (377.11497, 1.91)
Licochalcone A	Chalcone					
Licochalcone C	Chalcone					
Hispaglabridin B	Isoflavan	$C_{25}H_{26}O_4$	390.18311	391.19021 (391.19039, 0.70)	413.17218 (413.17233, 1.92)	429.14618 (429.14627, 0.91)
Hispaglabridin A	Isoflavan	$C_{25}H_{28}O_4$	392.19876	393.20599 (393.20604, 0.78)	415.18708 (415.18798, 3.13[a])	431.16180 (431.16192, 1.28)
Glabrol	Flavanone					
3–Hydroxyglabrol	Flavanone	$C_{25}H_{28}O_5$	408.19368	409.20078 (409.20095, 0.83)	431.18280 (431.18290, 1.09)	447.15666 (447.15683, 1.10)
Kanzonol Y	Dihydrochalcone	$C_{25}H_{30}O_5$	410.20932	411.21588 (411.21660, 1.03)	433.19842 (433.19855, 0.96)	449.17226 (449.17248, 1.42)
Licoagrodin	Biflavonoid	$C_{45}H_{44}O_9$	728.29854	729.30599 (729.30581, 1.35)	751.28665 (751.28776, 2.57[a])	767.26173 (767.26169, 1.49)
Liquiritin	Flavanone	$C_{21}H_{22}O_9$	418.12639	419.13344 (419.13366, 0.91)	441.11692 (441.11561, 2.98[a])	457.08939 (457.08954, 0.64)
Neoliquiritin	Flavanone					
Isoliquiritin	Chalcone					
Neoisoliquiritin	Chalcone					
Liquiritin apioside	Flavanone	$C_{26}H_{30}O_{13}$	550.16865	551.17602 (551.17592, 0.80)	573.15790 (573.15787, 0.53)	589.13179 (589.13180, 0.39)
Licuroside	Chalcone					
Schaftoside	Flavone	$C_{26}H_{28}O_{14}$	564.14791	565.15519 (565.15519, 0.57)	587.13713 (587.13713, 0.76)	603.11103 (603.11107, 0.59)
Isoschaftoside	Flavone					
Isoviolanthin	Flavone	$C_{27}H_{30}O_{14}$	578.16356	579.17089 (579.17084, 0.42)	601.15273 (601.15278, 0.47)	617.12662 (617.12672, 0.39)
Licorice saponin C2	Triterpene	$C_{42}H_{62}O_{15}$	806.40887	ND (807.41615, –)	829.39803 (829.39810, 1.32)	845.37210 (845.37203, 0.85)
Licorice saponin B2	Triterpene	$C_{42}H_{64}O_{15}$	808.42453	809.43171 (809.43180, 1.06)	831.41350 (831.41375, 0.94)	847.38671 (847.38768, 1.63)
22–Acetoxyglycyrrhizin	Triterpene	$C_{44}H_{64}O_{18}$	880.40927	ND (881.41655, –)	903.39803 (903.39849, 1.16)	919.37198 (919.37243, 1.06)
Licorice saponin A3	Triterpene	$C_{48}H_{72}O_{21}$	984.45679	985.46349 (985.46389, 1.39)	1007.44629 (1007.44584, 1.18)	1023.41932 (1023.41977, 0.63)

The *m/z* images were generated by using theoretical mass, with a bin width of ±5 ppm. ND, not detected. [a]RMS value higher than 2 ppm because of the low intensity of the specific adduct ion.

Cork
Cortex
Phloem rays
Phloem fibers
Cambium
Xylem rays
Xylem fibers
Vessels

250 µm   *m/z* 861.36695   *m/z* 325.14344   *m/z* 798.54096

Figure 3. MALDI images of a *Glycyrrhiza glabra* (licorice) rhizome section, recorded with a pixel size of 10 µm and 90 × 525 pixels in the image.
(a) Optical image.
(b) Glycyrrhizic acid (*m/z* 861.36695, K$^+$ adduct, RMS = 0.47 ppm).
(c) Glabridin (*m/z* 325.14344, protonated, RMS = 1.11 ppm).
(d) Phosphatidylcholine (PC) (34:1) (*m/z* 798.54096, K$^+$ adduct, RMS = 1.80 ppm). This assignment is not fully confirmed, as the protonated and sodium-attached isomers of PC(34:1) were not observed.

resolution. In Figure 3(d), a selected lipid was visualized uniquely in the cambium layer, which is a distinct layer separating the yellowish grey bark from the finely radiate yellow wood. The flavonoids imaged in Figure 2(b) only appear in the cork layer (as co-localized with glabridin) in the 10–µm resolution experiment (Figure S1). The antifungal activity of glabridin has been demonstrated earlier (Fatima *et al.*, 2009), and therefore the present results suggest that the tissue-specific localization of glabridin might contribute to its plant–pathogen interactions, for example, as the first chemical barrier against fungal pathogens in the soil.
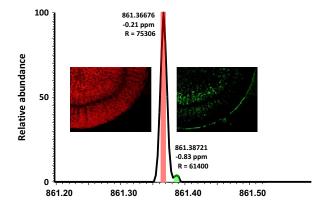
MALDI imaging of the licorice rhizome cross section at a spatial resolution of 10 µm also provided detailed morphological features at the cellular level. As marked by the red arrows in Figure 3(a) and (b), the vessels with an approximate diameter of 80 µm in the rhizome tissue are clearly resolved at this spatial resolution. Histological features are also visualized clearly by overlaying three ion images in one composite image (Figure 4b). Glabridin, glycyrrhizic acid and phosphatidylinositol (34:3) precisely represent the different histological regions and their fine structure. Mass spectrometric images can be directly correlated with anatomical features, as observed in the optical microscope image (Figure 4a). The combination of these histological features and all the chemical information present in the extracted images of secondary metabolites provides crucial hints to their metabolic origin, because plant secondary metabolites are more likely to be limited to certain regions of an organism than the primary metabolites are. Furthermore, the localization of certain classes of metabolites is beneficial for the optimization of the isolation process, as tissue-specific extraction can be applied in a more efficient screening for new compounds.

MS/MS imaging for image-assisted compound identification at high mass resolving power

The high mass resolving power and accuracy ensured that closely neighboring peaks, with the same nominal mass, were separated for the proper generation of selective ion images. In the highly resolved mass spectra, several pairs of peaks differing by <0.1 *m/z* units were observed. Figure 5 shows a mass spectrum from a rhizome cross section in a narrow mass window from *m/z* 861.30 to 861.40. Two different molecular species with a mass difference of 0.02098 mass units are clearly separated and assigned as the potassium adduct of GA and the sodium adduct of licorice saponin G2 (LS G2). The distribution of these two compounds is different in the rhizome, as seen in Figure 5. The localization of GA covers most areas of rhizome tissues, except the cambium layer. In contrast, the ion assigned as [LS G2 + Na]$^+$ is mainly found in the cork layer, and in phloem and xylem fibres, whereas it is absent in the central pith, and xylem and phloem rays, as well as

Figure 4. Correlation of histology and ion image in a *Glycyrrhiza glabra* (licorice) rhizome cross section at a spatial resolution of 30 µm.
(a) Optical image of one-quarter of the area of the tissue section.
(b) Overlay of ion images: red, *m/z* 325.14344 ([glabridin + H]$^+$, RMS = 0.85 ppm); blue, *m/z* 861.36695 ([GA + K]$^+$, RMS = 0.65 ppm); and green, *m/z* 871.47334 ([PI(34:3) + K]$^+$, RMS = 1.44 ppm).

Figure 5. Section of a single-pixel mass spectrum showing two peaks, the sodium-attached LS G2 (*m/z* 861.38793) and the potassium-attached GA (*m/z* 861.36695), with a mass difference of 0.02098 Da. The two ion images, GA (*m/z* 861.36645, RMS = 0.65 ppm, red) and LS G2 (*m/z* 861.38620, RMS = 1.87 ppm, green), were acquired with a spatial resolution of 30 μm and 205 × 255 pixels across the rhizome section. The ion images were generated with a bin width of ±5 ppm.

most of the parenchyma cells of the rhizome cortex. In order to resolve two such closely spaced isobars, a very narrow image bin width ($\Delta m/z = \pm 5$ ppm) was used. The advantage of the very high mass resolution was lost if a wide bin width of, for example, $\Delta m/z = 0.1$ was applied in the subsequent image processing, resulting in an overlay of several isobaric signals.

MS/MS imaging at a pixel size of 21 μm was conducted as a validation of the identities of these two particular compounds, supported by the similarities of ion distribution images of precursor and fragments. A quadrupole mass filter in the Q–Exactive was used for precursor ion selection at an isolation width of 0.9 u (unified atomic mass unit) for optimum sensitivity, and ion activation was performed in an high-energy collisional dissociation cell, resulting in fragments over a wide mass range. Two precursor ions of [GA + K]⁺ and [LS G2 + Na]⁺ with *m/z* values of 861.36695 and 861.38793, respectively, were thus isolated and fragmented together. The resulting product ion spectrum is found in Figure 6, along with the assignment of the various fragments, some of which are also very closely neighbored in mass, and in the corresponding MS/MS images. As can be seen, the product ion spectrum – a superposition of the product ion spectra of the two individual compounds – is quite complex, but the MS/MS images of the different fragments show quite clearly the two different distributions and thus also which of the two precursor ions (also presented in Figure 6) the different fragment ions belong to. The high signal intensity ion at nominal *m/z* 685 was resolved into two ions, *m/z* 685.33486 and 685.35583, which are explained as a loss of glucuronic acid from the two precursor ions. Likewise, the successive loss of another glucuronic acid group generated the ions at nominal *m/z* 509, which were separated by the high-resolution mass analyzer into

m/z 509.30277 and 509.32375, respectively. Another high signal intensity fragment ion at *m/z* 391.02733 was assigned as the potassium adduct of the di-glucuronide residue ion from [GA + K]⁺. The low intensity ion at *m/z* 375.05340 was assigned as the same residue of di-glucuronide present as the sodium adduct from [LS G2 + Na]⁺.

The MS/MS images in Figure 6 correspond very well to the distributions obtained in the full-scan experiment in Figure 5, confirming that full-scan imaging at very high mass resolution is sufficient to resolve even very closely neighbored isobars, but of course not compositional isomers. Furthermore, the fact that the MS/MS images are of similar quality as the full-scan images demonstrates the reliability and sensitivity of the MS/MS method of the instrumental set–up. It is not limited to certain peaks at high intensity, but is successfully achieved over almost the whole intensity range.

CONCLUSIONS

The AP-SMALDI10 imaging ion source coupled to the Q–Exactive Orbitrap mass spectrometer provides for high resolution and accuracy in mass and space. We have applied the set–up for the identification and localization of a number of natural products in cross sections of licorice rhizome, to provide examples of what is now possible with MS imaging of plant metabolites at this level. Our results clearly demonstrate the relevance of these features in the context of plant sciences, as the high spatial resolution made it possible to image morphological features in great detail, and the high spectral resolution was necessary in order to resolve a number of isobaric compounds present among the vast number of plant metabolites. The pixel size was not set to the smallest possible value (such as 3 μm, demonstrated recently for animal tissue imaging; Römpp and Spengler, 2013) in order to reduce measurements times. The selected pixel resolution of 10 μm, however, was found to be well adapted to the histological question.

We found that in the case of even very closely neighbored isobars (0.02 Da mass difference) the high mass resolving power was sufficient for selective imaging of each of the compounds, as validated with even more selective MS/MS images of the same two compounds. With the experiment set–up applied here, the full scan has the advantage of efficiency (many compounds imaged in one experiment) and sensitivity, whereas the MS/MS approach was not as sensitive on low-abundance compounds. In return, the MS/MS imaging analysis has the obvious advantage of structural information provided in the experiment, and the possibility of selective imaging of isomeric species.

With the significant technological improvements during the past decade, mass spectrometry-based imaging shows an efficient way in the dereplication of unknown bioactive natural products. A major advantage of this technology is the reduced degradation of metabolites normally observed
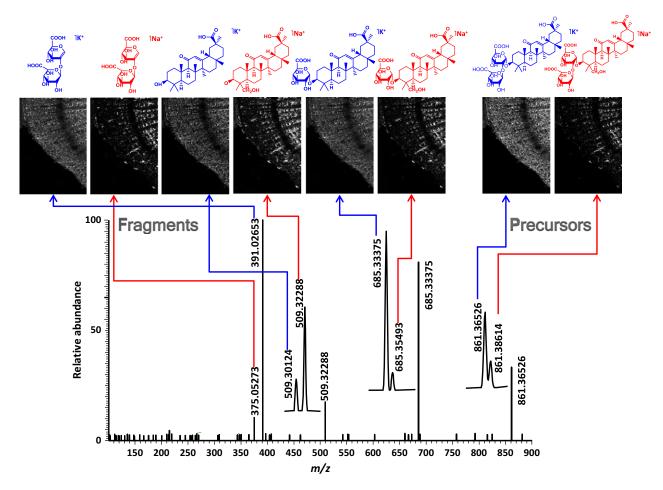
Figure 6. MS/MS images of two saponins in the *Glycyrrhiza glabra* (licorice) rhizome section, with a pixel size of 21 μm. The spectrum is a single-pixel MS/MS spectrum of the precursor *m/z* 861 (selection window 0.9 u), resulting in a superposition of the product ion spectra of the sodium adduct of LS G2 (*m/z* 861.38793) and the potassium adduct of GA (*m/z* 861.36695). The product ion images show distributions similar to the full-scan images in Figure 5.

in the course of extraction. In many cases, heat extraction or acidic and basic precipitations readily result in various artefacts, for example, in the hydrolysis of glycosides. High-resolution MS imaging will in the future greatly help us to visualize metabolites in different tissues and to obtain molecular information at the cellular level, ultimately helping us to further unravel the fate of metabolites and related physiological functions during plant growth.

EXPERIMENTAL PROCEDURES

Chemicals and plant samples

Trifluoroacetic acid (TFA), water (HPLC grade), acetone and 2,5–dihydroxybenzoic acid (DHB; 98%) were purchased from Fluka (now Sigma-Aldrich, http://www.sigmaaldrich.com). *Glycyrrhiza glabra* rhizomes were provided by the Botanical Garden of Frankfurt (http://www.botanischergarten-frankfurt.de).

Sample preparation

The fresh rhizomes were cleaned and stored at −80°C until use. For cryo-sectioning, the rhizomes were directly fixed on the sample holder of a cryo-microtome (HM 525 cryostat; Thermo Scien-

tific, http://www.thermoscientific.com), using water as the only adhesive. Sections (20–μm thick) were cut at −18°C and thaw-mounted on regular glass slides, which were stored at −80°C until analysis. On the day of analysis, the tissue sections were dehydrated in a vacuum desiccator prior to matrix application. A dedicated pneumatic sprayer (SMALDIPrep; TransMIT GmbH, http://www.transmit.de; Bouschen *et al.*, 2010) was used for the uniform application of a DHB matrix solution prepared at concentrations of 30 mg ml^{-1} in acetone/water (0.1% TFA) 1 : 1 v/v. The matrix crystals size and uniformity were checked before the measurements by visual inspection in an Olympus BX–40 microscope (Olympus, http://www.olympus-global.com). A uniform matrix layer and crystal size <10 μm were obtained, as needed for a MALDI imaging experiment at high spatial resolution. Optical images of tissue sections were taken before matrix application with the Olympus BX–40 microscope.

Instrumentation

All measurements were performed using the AP-SMALDI10 high-resolution MALDI imaging ion source (TransMIT GmbH), which was operated at atmospheric pressure and coupled to a Q–Exactive Orbitrap mass spectrometer (Thermo Fisher). The ion source includes a nitrogen laser (λ = 337 nm) operating at a repetition rate of 60 Hz. The laser beam was focused by a centrally bored

objective lens to an optical diameter of 8.4 μm ($1/e^2$ definition; Koestler *et al.*, 2008). For experiments at 30–μm pixel size, the laser was slightly defocused, and the laser energy was correspondingly increased in order to increase the irradiation area and thus the ion yield. For imaging at 10–μm pixel size a laser spot size of approximately 10 μm diameter was used. The effective diameter of the ablation spot varies with the chosen laser energy (Guenther *et al.*, 2010). For each mass spectrum, ions from 30 laser pulses were accumulated in the C–trap before being sent to the mass analyzer. All experiments were performed in the positive ion mode with the target voltage set to +4.3 kV. The step size of the sample stage was set to the desired pixel size. The measurement speed in full scan mode (scan range *m/z* 225–1040) was about 1.3 sec per pixel at a mass resolution of 140 000 (at *m/z* 200), including stage movement. Internal lock-mass calibration was used, providing a mass accuracy of better than 2 ppm over the course of the entire run. MS/MS imaging experiments were performed with an isolation width of 0.9 mass units. The pixel size was 21 μm, and an area of 3.8 × 5.4 mm was imaged. Additional non-imaging MS/MS measurements for compound identification were performed by line scanning over the sample.

Data processing

Ion images were generated with the imaging software package MIRI-ON (Paschke *et al.*, 2013). All images were generated with a bin width of ±5 ppm. The only processing of the images was the scaling of intensities in single ion images to the highest intensity measured for each ion separately. Overlain images were generated by using the signal intensities of three different compounds in the red, green and blue channel of an RGB image, respectively. Metabolites were identified in a combination of exact mass measurements, MS/MS experiments and by searching in the METLIN Metabolite Database (Smith *et al.*, 2005). The mass accuracy of metabolites in the imaging measurements was calculated as mass accuracy (ppm) in root mean square error (RMS) of the full measurement.

SUPPORTING INFORMATION

Additional Supporting Information may be found in the online version of this article.
Figure S1. MALDI images of a licorice rhizome section, recorded with a pixel size of 10 μm and with 90 × 525 pixels in the image.

REFERENCES

Abbott, E., Hall, D., Hamberger, B. and Bohlmann, J. (2010) Laser microdissection of conifer stem tissues: isolation and analysis of high quality RNA, terpene synthase enzyme activity and terpenoid metabolites from resin ducts and cambial zone tissue of white spruce (*Picea glauca*). *BMC Plant Biol.* **10**, 1–16.

Asl, M.N. and Hosseinzadeh, H. (2008) Review of pharmacological effects of *Glycyrrhiza* sp. and its bioactive compounds. *Phytother. Res.* **22**, 709–724.

Bjarnholt, N., Li, B., D'Alvise, J. and Janfelt, C. (2014) Mass spectrometry imaging of plant metabolites - principles and possibilities. *Nat. Prod. Rep.* **31**, 818–837.

Borisjuk, L., Rolletschek, H. and Neuberger, T. (2012) Surveying the plant's world by magnetic resonance imaging. *Plant J.* **70**, 129–146.

Bouschen, W., Schulz, O., Eikel, D. and Spengler, B. (2010) Matrix vapor deposition/recrystallization and dedicated spray preparation for high-resolution scanning microprobe matrix-assisted laser desorption/ionization imaging mass spectrometry (SMALDI-MS) of tissue and single cells. *Rapid Commun. Mass Spectrom.* **24**, 355–364.

Burrell, M., Earnshaw, C. and Clench, M. (2007) Imaging matrix assisted laser desorption ionization mass spectrometry: a technique to map plant metabolites within tissues at high spatial resolution. *J. Exp. Bot.* **58**, 757–763.

Campbell, D., Ferreira, C., Eberlin, L. and Cooks, R.G. (2012) Improved spatial resolution in the imaging of biological tissue using desorption electrospray ionization. *Anal. Bioanal. Chem.* **404**, 389–398.

Farag, M.A., Porzel, A. and Wessjohann, L.A. (2012) Comparative metabolite profiling and fingerprinting of medicinal licorice roots using a multiplex approach of GC–MS, LC–MS and 1D NMR techniques. *Phytochemistry*, **76**, 60–72.

Fatima, A., Gupta, V.K., Luqman, S., Negi, A.S., Kumar, J.K., Shanker, K., Saikia, D., Srivastava, S., Darokar, M.P. and Khanuja, S.P.S. (2009) Antifungal activity of *Glycyrrhiza glabra* extracts and its active constituent glabridin. *Phytother. Res.* **23**, 1190–1193.

Fenwick, G.R., Lutomski, J. and Nieman, C. (1990) Licorice, *Glycyrrhiza-Glabra* L – composition, uses and analysis. *Food Chem.* **38**, 119–143.

Graham, T.L., Kim, J.E. and Graham, M.Y. (1990) Role of constitutive isoflavone conjugates in the accumulation of glyceollin in soybean infected with phytophthora-megasperma. *Mol. Plant Microbe Interact.* **3**, 157–166.

Guenther, S., Koestler, M., Schulz, O. and Spengler, B. (2010) Laser spot size and laser power dependence of ion formation in high resolution MALDI imaging. *Int. J. Mass Spectrom.* **294**, 7–15.

Guerquin-Kern, J.-L., Wu, T.-D., Quintana, C. and Croisy, A. (2005) Progress in analytical imaging of the cell by dynamic secondary ion mass spectrometry (SIMS microscopy). *Biochim. Biophys. Acta* **1724**, 228–238.

Hayashi, H. (2009) Molecular biology of secondary metabolism: case study for *Glycyrrhiza* plants. In *Recent Advances in Plant Biotechnology* (Kirakosyan, A. and Kaufman, P.B., eds). New York, NY: Springer US, pp. 89–103.

Hayashi, H., Fukui, H. and Tabata, M. (1988) Examination of triterpenoids produced by callus and cell suspension cultures of *Glycyrrhiza glabra*. *Plant Cell Rep.* **7**, 508–511.

Hayashi, H., Hiraoka, N., Ikeshiro, Y. and Yamamoto, H. (1996) Organ specific localization of flavonoids in *Glycyrrhiza glabra* L. *Plant Sci.* **116**, 233–238.

Jensen, W.A. (1962) *Botanical Histochemistry*. San Francisco & London: WH Freeman & Co.

Jun, J.H., Song, Z., Liu, Z., Nikolau, B.J., Yeung, E.S. and Lee, Y.J. (2010) High-spatial and high-mass resolution imaging of surface metabolites of arabidopsis thaliana by laser desorption-ionization mass spectrometry using colloidal silver. *Anal. Chem.* **82**, 3255–3265.

Kaspar, S., Peukert, M., Svatos, A., Matros, A. and Mock, H-P. (2011) MALDI-imaging mass spectrometry - An emerging technique in plant biology. *Proteomics*, **11**, 1840–1850.

Koestler, M., Kirsch, D., Hester, A., Leisner, A., Guenther, S. and Spengler, B. (2008) A high-resolution scanning microprobe matrix-assisted laser desorption/ionization ion source for imaging analysis on an ion trap/Fourier transform ion cyclotron resonance mass spectrometer. *Rapid Commun. Mass Spectrom.* **22**, 3275–3285.

Lee, Y.J., Perdian, D.C., Song, Z.H., Yeung, E.S. and Nikolau, B.J. (2012) Use of mass spectrometry for imaging metabolites in plants. *Plant J.* **70**, 81–95.

Li, B., Bjarnholt, N., Hansen, S.H. and Janfelt, C. (2011) Characterization of barley leaf tissue using direct and indirect desorption electrospray ionization imaging mass spectrometry. *J. Mass Spectrom.* **46**, 1241–1246.

Li, B., Hansen, S.H. and Janfelt, C. (2013) Direct imaging of plant metabolites in leaves and petals by Desorption Electrospray Ionization mass spectrometry. *Int. J. Mass Spectrom.* **348**, 15–22.

Liang, Z.T., Sham, T.T., Yang, G.Y., Yi, L., Chen, H.B. and Zhao, Z.Z. (2013) Profiling of secondary metabolites in tissues from *Rheum palmatum* L.

using laser microdissection and liquid chromatography mass spectrometry. *Anal. Bioanal. Chem.* **405**, 4199–4212.

Paschke, C., Leisner, A., Hester, A., Maass, K., Guenther, S., Bouschen, W. and Spengler, B. (2013) Mirion–a software package for automatic processing of mass spectrometric images. *J. Am. Soc. Mass Spectrom.* **24**, 1296–1306.

Ramos-Vara, J.A. (2005) Technical Aspects of Immunohistochemistry. *Vet. Pathol. Online* **42**, 405–426.

Robinson, S., Warburton, K., Seymour, M., Clench, M. and Thomas-Oates, J. (2007) Localization of water-soluble carbohydrates in wheat stems using imaging matrix-assisted laser desorption ionization mass spectrometry. *New Phytol.* **173**, 438–444.

Rogers, G.E. (1953) The localization of dehydrogenase activity and sulphydryl groups in wool and hair follicles by the use of tetrazolium salts. *Q. J. Microsc. Sci.* **94**, 253–268.

Römpp, A. and Spengler, B. (2013) Mass spectrometry imaging with high resolution in mass and space. *Histochem. Cell Biol.* **139**, 759–783.

Römpp, A., Guenther, S., Schober, Y., Schulz, O., Takats, Z., Kummer, W. and Spengler, B. (2010) Histology by mass spectrometry: label-free tissue characterization obtained from high-accuracy bioanalytical imaging. *Angew. Chem. Int. Ed. Engl.* **49**, 3834–3838.

Schober, Y., Guenther, S., Spengler, B. and Römpp, A. (2012) Single cell matrix-assisted laser desorption/ionization mass spectrometry imaging. *Anal. Chem.* **84**, 6293–6297.

Schwamborn, K. and Caprioli, R.M. (2010) Molecular imaging by mass spectrometry–looking beyond classical histology. *Nat. Rev. Cancer* **10**, 639–646.

Shan, S.J., Tanaka, H., Hayashi, J. and Shoyama, Y. (2001) Western blotting of glycyrrhetinic acid glucuronides using anti-glycyrrhizin monoclonal antibody. *J. Liq. Chromatogr. Rel. Technol.* **24**, 1491–1499.

Smith, C.A., O'Maille, G., Want, E.J., Qin, C., Trauger, S.A., Brandon, T.R., Custodio, D.E., Abagyan, R. and Siuzdak, G. (2005) METLIN - A metabolite mass spectral database. *Ther. Drug Monit.* **27**, 747–751.

Spengler, B., Hubert, M. and Kaufmann, R. (1994) MALDI ion imaging and biological ion imaging with a new scanning UV-laser microprobe. In *Proceedings of the 42nd ASMS Conference on Mass Spectrometry and Allied Topics*. Chicago, IL, pp. 1041.

Stafford, H.A. (1997) Roles of flavonoids in symbiotic and defense functions in legume roots. *Bot. Rev.* **63**, 27–39.

Svatoš, A. and Mock, H.-P. (2013) MALDI mass spectrometric imaging of plants. In *The Handbook of Plant Metabolomics* (Weckwerth, W. and Kahl, G., eds). Weinheim, Germany: Wiley-VCH Verlag GmbH & Co. KGaA, pp. 93–110.

Tani, T., Katsuki, T., Kubo, M. and Arichi, S. (1985) Histochemistry .7. Flavones in Scutellariae Radix. *Chem. Pharm. Bull. (Tokyo)* **33**, 4894–4900.

Tani, T., Katsuki, T., Kubo, M. and Arichi, S. (1986) Histochemistry (VIII). Distribution of starch and isoflavones in Pueraria radix. *Shoyakugaku Zasshi,* **40**, 247–251.

Walker, R.P., Chen, Z.H., Johnson, K.E., Famiani, F., Tecsi, L. and Leegood, R.C. (2001) Using immunohistochemistry to study plant metabolism: the examples of its use in the localization of amino acids in plant tissues, and of phosphoenolpyruvate carboxykinase and its possible role in pH regulation. *J. Exp. Bot.* **52**, 565–576.

Yamamoto, H., Ichimura, M., Ishikawa, N., Tanaka, T., Iinuma, M. and Mizuno, M. (1992) Localization of prenylated flavonoids in sophora-flavescens var angustifolia plants. *Z. Naturforsch. C* **47**, 535–539.

Ye, H., Gemperline, E., Venkateshwaran, M., Chen, R., Delaux, P.-M., Howes-Podoll, M., Ané, J.-M. and Li, L. (2013) MALDI mass spectrometry-assisted molecular imaging of metabolites during nitrogen fixation in the Medicago truncatula–Sinorhizobium meliloti symbiosis. *Plant J.* **75**, 130–145.

Yi, L., Liang, Z.-T., Peng, Y., Yao, X., Chen, H.-B. and Zhao, Z.-Z. (2012) Tissue-specific metabolite profiling of alkaloids in Sinomenii Caulis using laser microdissection and liquid chromatography–quadrupole/time of flight-mass spectrometry. *J. Chromatogr. A* **1248**, 93–103.